

Vladislav Gavrilets

Contents

15.1 Introduction 280

15.2 Helicopter Parameters 282

15.3 Equations of Motion 284

15.4 Component Forces and Moments 285

 15.4.1 Main Rotor Forces and Moments 285

 15.4.2 Engine, Governor, and Rotor Speed Model 295

 15.4.3 Fuselage Forces 298

 15.4.4 Vertical Fin Forces and Moments 299

 15.4.5 Horizontal Stabilizer Forces and Moments 300

 15.4.6 Tail Rotor 300

15.5 Actuator Models 304

References 305

Abstract

A nonlinear dynamic model of a miniature aerobatic helicopter is presented in detail. A component buildup was applied in devising the model, using simplified analytical expressions for the component forces and moments. Flight-test experiments were used to estimate several key parameters, such as the equivalent torsional stiffness in the hub. The model was used to design control logic for aerobatic maneuvers performed entirely under computer control.

V. Gavrilets
Flight Control and Navigation Group, Rockwell Collins Control Technologies, Warrenton,
VA, USA
e-mail: vgavrile@rockwellcollins.com

15.1 Introduction

Miniature helicopters with hingeless rotors are extremely agile compared to their full-scale counterparts due to fast shrinking of moments of inertia with size and therefore growth of control authority Mettler (2002). These vehicles can be used for tasks requiring aggressive maneuvering, such as pursuit and evasion in urban or mountainous environment, or aerial stunts for movie industry. Precise autonomous execution of aggressive maneuvers, coupled with online motion planning, can further expand utility of agile miniature rotorcraft. This created the need for an adequate nonlinear model of an aerobatic miniature helicopter.

An extensive body of literature has been devoted to the dynamics of full-scale helicopters, and step-by-step procedures for creating a first-principles dynamic model were outlined (Padfield 1996; Bramwell 2001; Talbot et al. 1982). Frequency-domain system identification techniques are widely used to evaluate accuracy of linearized models at different operating conditions (NASA Ames Research Center 2000; Tischler 1996). Due to a wide range of flow conditions and their complex interaction with the wake, cross-axis coupling in the hub, and sometimes interaction of the structural modes with the rigid body modes, the models of full-scale helicopters used in simulators tend to be complex and contain a large number of states.

Recent years have seen an increase in modeling efforts for small-scale helicopters. Mettler (2002) performed a comprehensive study of the features common to the dynamics of small-scale helicopters and applied frequency-domain methods for identification of linearized models. Most of the small-scale helicopters have Bell-Hiller stabilizer bars, which slow down rotor dynamics and mitigate gust response. It was shown (Mettler 2002) that this creates relatively low-frequency lateral and longitudinal pendulum-like flapping modes, which involve fuselage, rotor, and stabilizer bar. The same effect was observed on a full-size UH-1H helicopter, equipped with a stabilizer bar with mechanical dampers instead of aerodynamic surfaces. The modes are lightly damped and must be accounted for to develop a high-bandwidth control system required for autonomous aggressive maneuvering.

LaCivita et al. (2002b) developed a technique for integrating first-principles modeling and frequency-domain system identification to yield a nonlinear model for small-scale helicopters. The resulting model of the Yamaha R-50 helicopter employed 30 states and was used for H_∞ -based control system design for the helicopter in steady-state hovering or slow forward and backward flight (LaCivita et al. 2002a). The authors further compared accuracy of full linearized models and reduced-order linear models and came to similar conclusions with those previously noted by Mettler (2002), which advocated the use of first-order models for tip-path-plane flapping dynamics.

Abbeel et al. (2006) built a nonlinear model of a small-scale aerobatic helicopter, using a combination of first-principles modeling and data fitting based on reinforcement learning. The model used fewer states than the one described in this chapter: it included rigid body states and main rotor speed only. The authors used the model and apprenticeship learning algorithms to develop control laws that enabled tracking

of highly aggressive aerobatic trajectories (Abbeel et al. 2010) and autonomous autorotation landing (Abbeel et al. 2008). Under this approach, time histories from aerobatic flights conducted by an expert pilot were used to refine the model and tailor control law parameters to a particular task.

This chapter presents a development of a first-principles-based nonlinear dynamic model of a miniature helicopter, which proved sufficiently accurate to predict helicopter dynamics in a wide range of conditions, including aerobatic flight. This work is closely based on a modeling chapter in the author's doctoral dissertation (Gavrilets 2003), devoted to human-inspired approach to autonomous helicopter aerobatics. Most of the model parameters were measured directly, and several were estimated using data from flight-test experiments. Analytical linearization of the model with respect to forward speed yields simple models, directly used for design of feedback control laws for autonomous execution of aerobatic maneuvers. The helicopter used in the study is X-Cell .60 SE by Miniature Aircraft (1999), equipped with a 0.90 size engine and an electronic governor. This helicopter features a particularly stiff hub, which gives large control authority to cyclic actuators. The coupling in the hub for this helicopter was also shown to be negligible, which further simplified model development.

The helicopter flew a fully autonomous mission that included an axial roll, a hammerhead, and a Split-S and sequences of these maneuvers (Gavrilets et al. 2002). An artist representation of a Split-S maneuver is shown in Fig. 15.1. The state trajectories in both open loop and closed loop flights were well predicted by the nonlinear model that used a single set of parameters, invariant of the task being performed.

The work on the dynamic model was performed using a custom-designed and built avionics suite, which was concurrently developed. The avionics suite is described in detail in the author's Ph.D. dissertation (Gavrilets 2003).

The model has typical rigid body states with the quaternion attitude representation used in order to enable simulation of extreme attitudes (Rolfe and Staples 1986), two states for the lateral and longitudinal flapping angles, one for the rotor speed, and one for the integral of the rotor speed tracking error. This last state comes from the governor action, modeled with a proportional-integral feedback from the rotor speed tracking error to the throttle command. The model covers a large portion of the X-Cell's natural flight envelope: from hover flight to about 20 m/s forward flight. The maximum forward speed corresponds to an advance ratio $\mu = 0.15$, which is considered as relatively low (Padfield 1996), and permits a number of assumptions (e.g., thrust perpendicular to the rotor disk; see Chen (1979)). The cross-coupling effects in the rotor hub were also shown to be negligible for this helicopter, which further simplified model development. The mathematical model was developed using basic helicopter theory, accounting for the particular characteristics of a miniature helicopter. Most of the parameters were measured directly, and several were estimated using data collected from simple flight-test experiments, involving step and pulse responses in various actuator inputs. No formal system identification procedures are required for the proposed model structure. The model's accuracy was verified using comparison between model predicted responses and responses

Fig. 15.1 Miniature helicopter undergoing a Split-S maneuver. The same maneuver was performed fully autonomously under control laws, developed based on the dynamic model described in this chapter (Drawing courtesy of Popular Mechanics magazine)



collected during flight-test data. The model was also “flown” in simulator by an expert RC pilot to determine how well it reproduces the piloted flying qualities.

Analytical linearization of the model with respect to forward speed was used to derive simple linear models. These were subsequently used for a model-based design of the controllers used for the automatic execution of aerobatic maneuvers. The actual aggressive trajectories flown by the helicopter were adequately predicted by the simulation based on the developed nonlinear model.

The remainder of the chapter contains a full list of model parameters with the numerical values, dynamics equations of motion, and expressions for forces and moments exerted on the helicopter by its components. Flight-test data used to validate the model for various flight regimes, including aerobatics, is provided throughout the chapter.

15.2 Helicopter Parameters

The physical helicopter parameters used for the model are given in Table 15.1. The moments of inertia around the aircraft body axes passing through the vehicle center of gravity were determined using torsional pendulum tests (Harris 1996). The cross-axis moments of inertia are hard to measure without a balancing device, and since they are usually small, they were neglected. The X-Cell main and tail rotors, as well as the stabilizer bar, have symmetric airfoils. The lift curve slopes of these surfaces were estimated according to their respective aspect ratios (Kuethe and Chow 1986).

Table 15.1 Parameters of MIT instrumented X-Cell 60 SE helicopter

Parameter	Description
$m = 8.2 \text{ kg}$	Helicopter mass
$I_{xx} = 0.18 \text{ kg m}^2$	Rolling moment of inertia
$I_{yy} = 0.34 \text{ kg m}^2$	Pitching moment of inertia
$I_{zz} = 0.28 \text{ kg m}^2$	Yawing moment of inertia
$K_\beta = 54 \text{ N-m/rad}$	Hub torsional stiffness
$\gamma_{fb} = 0.8$	Stabilizer bar Lock number
$B_{\delta_{lat}}^{\text{nom}} = 4.2 \text{ rad/rad}$	Lateral cyclic to flap gain at nominal rpm
$A_{\delta_{lon}}^{\text{nom}} = 4.2 \text{ rad/rad}$	Longitudinal cyclic to flap gain at nominal rpm
$K_\mu = 0.2$	Scaling of flap response to speed variation
$\Omega_{\text{nom}} = 167 \text{ rad/s}$	Nominal m.r. speed
$R_{\text{mr}} = 0.775 \text{ m}$	m.r. radius
$c_{\text{mr}} = 0.058 \text{ m}$	m.r. chord
$a_{\text{mr}} = 5.5 \text{ rad}^{-1}$	m.r. blade lift curve slope
$C_{D_0}^{\text{mr}} = 0.024$	m.r. blade zero lift drag coefficient
$C_{T_{\text{max}}}^{\text{mr}} = 0.0055$	m.r. max thrust coefficient
$I_{\beta_{\text{mr}}} = 0.038 \text{ kg m}^2$	m.r. blade flapping inertia
$R_{\text{tr}} = 0.13 \text{ m}$	t.r. radius
$c_{\text{tr}} = 0.029 \text{ m}$	t.r. chord
$a_{\text{tr}} = 5.0 \text{ rad}^{-1}$	t.r. blade lift curve slope
$C_{D_0}^{\text{tr}} = 0.024$	t.r. blade zero lift drag coefficient
$C_{T_{\text{max}}}^{\text{tr}} = 0.05$	t.r. max thrust coefficient
$n_{\text{tr}} = 4.66$	Gear ratio of t.r. to m. r.
$n_{\text{es}} = 9.0$	Gear ratio of engine shaft to m. r.
$\delta_r^{\text{trim}} = 0.1 \text{ rad}$	t.r. pitch trim offset
$S_{\text{vf}} = 0.012 \text{ m}^2$	Effective vertical fin area
$C_{L_{\alpha}}^{\text{vf}} = 2.0 \text{ rad}^{-1}$	Vertical fin lift curve slope
$\epsilon_{\text{vf}}^{\text{tr}} = 0.2$	Fraction of vertical fin area exposed to t.r. induced velocity
$S_{\text{ht}} = 0.01 \text{ m}^2$	Horizontal fin area
$C_{L_{\alpha}}^{\text{ht}} = 3.0 \text{ rad}^{-1}$	Horizontal tail lift curve slope
$P_{\text{eng}}^{\text{idle}} = 0.0 \text{ W}$	Engine idle power
$P_{\text{eng}}^{\text{max}} = 2,000.0 \text{ W}$	Engine max power
$K_p = 0.01 \text{ s/rad}$	Proportional governor gain
$K_i = 0.02 \text{ 1/rad}$	Integral governor gain
$S_x^{\text{fus}} = 0.1 \text{ m}^2$	Frontal fuselage drag area
$S_y^{\text{fus}} = 0.22 \text{ m}^2$	Side fuselage drag area
$S_z^{\text{fus}} = 0.15 \text{ m}^2$	Vertical fuselage drag area
$h_{\text{mr}} = 0.235 \text{ m}$	m.r. hub height above c.g.
$l_{\text{tr}} = 0.91 \text{ m}$	t.r. hub location behind c.g.
$h_{\text{tr}} = 0.08 \text{ m}$	t.r. height above c.g.
$l_{\text{ht}} = 0.71 \text{ m}$	Stabilizer location behind c.g.

The effective torsional stiffness in the hub was estimated from angular rate responses to step commands in cyclic, as described in Sect. 15.4.1.3.

Note that in the table, “m.r.” stands for the main rotor, and “t.r.” stands for the tail rotor.

15.3 Equations of Motion

The rigid body equations of motion for a helicopter are given by the Newton-Euler equations shown below. Here the cross products of inertia are neglected:

$$\dot{u} = vr - wq - g \sin \theta + (X_{mr} + X_{fus}) / m$$

$$\dot{v} = wp - ur + g \sin \phi \cos \theta + (Y_{mr} + Y_{fus} + Y_{tr} + Y_{vf}) / m$$

$$\dot{w} = uq - vp + g \cos \phi \cos \theta + (Z_{mr} + Z_{fus} + Z_{ht}) / m$$

$$\dot{p} = qr(I_{yy} - I_{zz}) / I_{xx} + (L_{mr} + L_{vf} + L_{tr}) / I_{xx}$$

$$\dot{q} = pr(I_{zz} - I_{xx}) / I_{yy} + (M_{mr} + M_{ht}) / I_{yy}$$

$$\dot{r} = pq(I_{xx} - I_{yy}) / I_{zz} + (-Q_e + N_{vf} + N_{tr}) / I_{zz}$$

The set of forces and moments acting on the helicopter are organized by components: $()_{mr}$ for the main rotor, $()_{tr}$ for the tail rotor, $()_{fus}$ for the fuselage (includes fuselage aerodynamic effects), $()_{vf}$ for the vertical fin, and $()_{ht}$ for the horizontal stabilizer. These forces and moments are shown along with the main helicopter variables in Fig. 15.2. Q_e is the torque produced by the engine to counteract the aerodynamic torque on the main rotor blades. The helicopter blades rotate clockwise when viewed from above; therefore, $Q_e \geq 0$. In the above equations, it was assumed that the fuselage center of pressure coincides with the c.g.; therefore, the moments created by the fuselage aerodynamic forces were neglected.

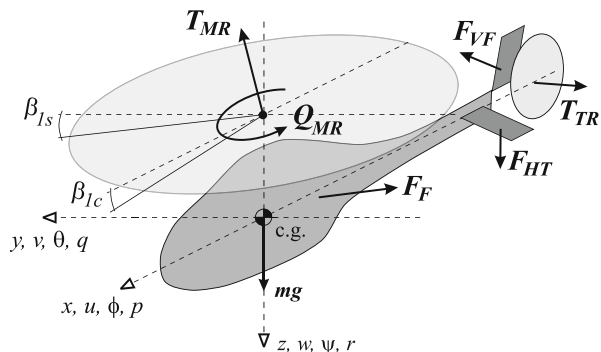


Fig. 15.2 Moments and forces acting on helicopter

The rotational kinematic equations were mechanized using quaternions (Rolfe and Staples 1986). The inertial velocities are derived from the body-axis velocities by a coordinate transformation (flat-Earth equations are used) and integrated to obtain inertial position. A fourth-order Runge-Kutta integration method is used, with an integration step of 0.01 s.

15.4 Component Forces and Moments

15.4.1 Main Rotor Forces and Moments

15.4.1.1 Thrust

For the main rotor thrust, it was assumed that the inflow is steady and uniform. According to Padfield (1996, p. 126), the time constant for settling of the inflow transients at hover is given by

$$\tau_\lambda = \frac{0.849}{4\lambda_{\text{trim}}\Omega_{\text{mr}}} \quad (15.1)$$

Induced velocity at hover trim condition can be determined from simple momentum theory:

$$V_{\text{imr}} = \sqrt{\frac{mg}{2\rho\pi R_{\text{mr}}^2}} = 4.2 \text{ m/s} \quad (15.2)$$

The tip speed of the main rotor is $V_{\text{mr}}^{\text{tip}} = \Omega_{\text{mr}} R_{\text{mr}} = 125.7 \text{ m/s}$, from which the inflow ratio is $\lambda_{\text{imr}} = V_{\text{imr}}/V_{\text{mr}}^{\text{tip}} = 0.033$. Therefore, the time it takes for the inflow to settle is $\tau_\lambda = 0.038 \text{ s}$, which is significantly faster than the rigid body dynamics. During the maneuvers requiring large thrust variations, the time constant may change substantially. However, as shown in the section on the main rotor flapping dynamics, the X-Cell cyclic control authority is dominated by the hub torsional stiffness, which makes the modeling of the inflow transients less critical.

A momentum theory-based iterative scheme given by Padfield (1996, p. 123) was adapted to compute the thrust coefficient and inflow ratio as a function of airspeed, rotor speed, and collective setting. Flapping angles were neglected in the computation of the rotor thrust. The blades of the main rotor have no twist. The influence of the cyclics and the roll rate on thrust are of second order for advance ratio range $\mu < 0.15$ and were neglected as well. An empirically determined maximum thrust coefficient was introduced, since momentum theory does not take into account the effect of blade stall.

The thrust coefficient is given by (omitting the “mr” index)

$$C_T = \frac{T}{\rho (\Omega R)^2 \pi R^2} \quad (15.3)$$

where T is the main rotor thrust. Then, the following system of equations can be solved iteratively:

$$\lambda_0 = \frac{C_T}{2\eta_w \sqrt{\mu^2 + (\lambda_0 - \mu_z)^2}} \quad (15.4)$$

$$C_T^{\text{ideal}} = \frac{a\sigma}{2} \left(\theta_0 \left(\frac{1}{3} + \frac{\mu^2}{2} \right) + \frac{\mu_z - \lambda_0}{2} \right) \quad (15.5)$$

$$C_T = \begin{cases} C_T^{\text{ideal}} & \text{if } -C_T^{\text{max}} \leq C_T^{\text{ideal}} \leq C_T^{\text{max}} \\ -C_T^{\text{max}} & \text{if } C_T^{\text{ideal}} < -C_T^{\text{max}} \\ C_T^{\text{max}} & \text{if } C_T^{\text{max}} < C_T^{\text{ideal}} \end{cases} \quad (15.6)$$

$$C_T^{\text{max}} = \frac{T^{\text{max}}}{\rho (\Omega R)^2 \pi R^2} \quad (15.7)$$

Here

$$\mu = \frac{\sqrt{(u - u_{\text{wind}})^2 + (v - v_{\text{wind}})^2}}{\Omega R} - \text{advance ratio}$$

$$\mu_z = \frac{w - w_{\text{wind}}}{\Omega R} - \text{normal airflow component}$$

$$\sigma = \frac{2c}{\pi R} - \text{solidity ratio}$$

a – lift curve slope

θ_0 – commanded collective angle

η_w – coefficient of nonideal wake contraction

$T^{\text{max}} = 2.5 \text{ mg}$ – maximum rotor thrust

Based on momentum theory, the rotor wake far downstream contracts by a factor of 2 (Padfield 1996, p. 116). A coefficient η_w was introduced to account for nonideal wake contraction and the power lost due to the nonuniform velocity and pressure distribution in the wake. An approximate value for this coefficient was determined to be $\eta_w = 0.9$. Hence, the iterative scheme given in Padfield (1996, p. 123) is modified as follows. First, define the zero function:

$$g_0 = \lambda_0 - \frac{C_T}{2\eta_w \Lambda^{1/2}}, \text{ where}$$

$$\Lambda = \mu^2 + (\lambda_0 - \mu_z)^2$$

and thrust coefficient C_T is given by Eq. (15.5). Apply Newton's iterative scheme:

$$\lambda_{0_{j+1}} = \lambda_{0_j} + f_j h_j (\lambda_{0_j})$$

$$h_j = - \left(\frac{g_0}{dg_0/d\lambda_0} \right)_{\lambda_0=\lambda_{0_j}}$$

An explicit expression for h_j :

$$h_j = - \frac{(2\eta_w \lambda_{0_j} \Lambda^{1/2} - C_T) \Lambda}{2\eta_w \Lambda^{3/2} + \frac{a\sigma}{4} \Lambda - C_T (\mu_z - \lambda_{0_j})}$$

Padfield (1996, p. 123) suggests a constant value of the convergence rate coefficient $f_j = 0.6$.

Note that at hover the denominator of Eq. (15.4) is zero when the vertical velocity is equal to the inflow velocity. This condition corresponds to a vortex-ring state, which cannot be modeled adequately by the momentum theory. Instead, the denominator is numerically separated from zero. In general, this condition is avoided in flight because it leads to a loss of control. One has to keep in mind that the simulation does not adequately represent the helicopter dynamics when vortex-ring conditions exist on either the main or the tail rotor. Furthermore, strictly speaking, the momentum theory applies only to a fully developed steady-state flow in ascending flight. Empirical corrections for descending flight, cited by Padfield (1996, p. 118), could be used to make thrust prediction somewhat more accurate.

The momentum theory approach was previously shown to be adequate for estimating steady-state main rotor thrust both at hover and in fast forward flight. Results of the wind tunnel tests with a 5-ft-diameter rotor are given by Harris (1972) and summarized by Bramwell (2001, pp. 109–114). It was shown that the blade lift curve slope coefficient a can be determined from experiments such that the momentum theory accurately predicts thrust for a wide range of advance ratios and collective pitch angles. To test the applicability of momentum theory-based thrust calculation to transient response, flight data was gathered for collective pitch pulse responses at hover. At hover, the vertical acceleration can be represented by a linear relation:

$$a_z = Z_w w + Z_{\text{col}} \delta_{\text{col}} \quad (15.8)$$

The vertical speed damping stability derivative Z_w and the collective pitch control derivative Z_{col} can be obtained analytically by linearization of the momentum theory equations (Padfield 1996, pp. 219, 229). For hover,

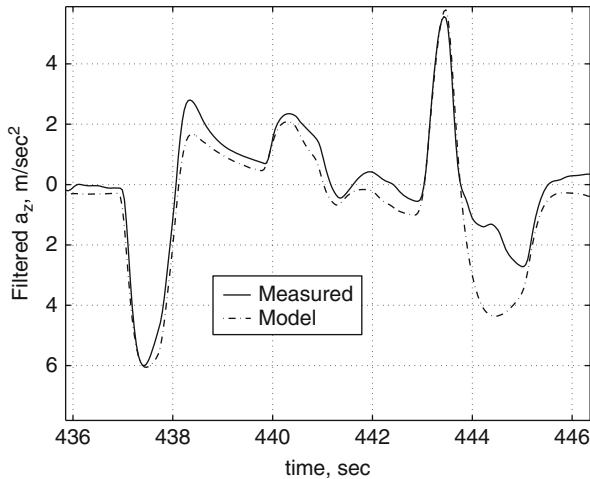


Fig. 15.3 Modeling vertical acceleration response at hover

$$Z_w = -\frac{\rho (\Omega R) \pi R^2}{m} \frac{2a\sigma\lambda_0}{16\lambda_0 + a\sigma} \quad (15.9)$$

$$Z_{col} = -\frac{\rho (\Omega R)^2 \pi R^2}{m} \frac{8}{3} \frac{a\sigma\lambda_0}{16\lambda_0 + a\sigma} \quad (15.10)$$

The same value for the blade lift curve slope was used as the one determined for the particular airfoil used in the tests summarized by Harris (1972), $a = 5.5$. This value is consistent with the high aspect ratio of the main rotor blades, if the blades are considered as a wing (Kuethe and Chow 1986). The mean values were subtracted from the collective command and the vertical acceleration measurement; the signals were filtered with a first-order low-pass filter with time constant of 0.2 s. The digital models of the analog low-pass filter and the servomechanism were applied to the collective command for consistency. Figure 15.3 shows the comparison of the computed vertical acceleration from Eq. (15.8) and actual acceleration. As can be seen, the model, based on linearization of the momentum theory, agrees well with flight data.

15.4.1.2 Torque

The main rotor torque can be approximated as a sum of induced torque due to generated thrust and torque due to profile drag on the blades (Padfield 1996, p. 116):

$$C_Q = \frac{Q}{\rho (\Omega R)^2 \pi R^3} = C_T (\lambda_0 - \mu_z) + \frac{C_{D_0}\sigma}{8} \left(1 + \frac{7}{3}\mu^2\right) \quad (15.11)$$

where C_Q is the torque coefficient and C_{D_0} is the profile drag coefficient of the main rotor blade. The profile drag is not significantly affected by changes in the collective setting. Thus, the yawing moment produced by the main rotor is given by

$$Q_{mr} = C_Q \rho (\Omega R)^2 \pi R^3 \quad (15.12)$$

Profile drag coefficient of the main rotor blade was estimated as $C_{D_0} = 0.024$. Underestimation of the profile drag coefficient would lead to overprediction of the main rotor speed in windmilling flight conditions, which occur during autorotation and some agile maneuvers.

Except for the hover condition, the rotor in-plane force, which contributes to the drag and side force, is substantially smaller than the drag provided by the fuselage and the side force from the fuselage and the empennage. This force was neglected in the calculations; effectively it was lumped with the fuselage forces, estimated in Sect. 15.4.3. The moments due to the in-plane force are much smaller than those due to the blade flapping, since the torsional stiffness of the hub retention is high on the X-Cell.

15.4.1.3 Main Rotor Moments and Flapping Dynamics

The main rotor flapping angle β can be represented as a Fourier series of the blade azimuth angle ψ , with only the first three coefficients retained (Padfield 1996, p. 32):

$$\beta(\psi) = a_0 + a_1 \cos \psi + b_1 \sin \psi \quad (15.13)$$

Flapping of the teetering stabilizer bar can be represented by a similar equation without the constant term since no coning takes place:

$$\beta_s(\psi) = a_{1s} \sin \psi + b_{1s} \cos \psi \quad (15.14)$$

Stabilizer bar flapping contributes to the change of the main rotor blade pitch angle through a mechanical linkage:

$$\theta(\psi) = \theta_0 + \theta_{lon} \sin \psi + \theta_{lat} \cos \psi + k_s \beta_s \quad (15.15)$$

The swashplate deflections change the cyclic pitch angle of both the main rotor and the stabilizer bar. Coupled second-order differential equations can be developed for Fourier coefficients of the main rotor and stabilizer bar flapping. It can be shown (Padfield 1996, pp. 33–35) that the undamped natural frequency of the flapping motion is close to the rotor speed Ω_{mr} and the damping ratio can be approximated by $\gamma/8$, where γ is the Lock number of the blades being considered (main rotor or stabilizer bar). The Lock number represents the ratio of aerodynamic to inertial forces and is defined as

$$\gamma = \frac{\rho c a R^4}{I_\beta} \quad (15.16)$$

For the main rotor blades, the Lock number is relatively high, $\gamma_{mr} \approx 3.7$; therefore, the flapping motion is well damped. For a step response, this corresponds to the settling time (to within 5 % of the steady-state value) of $24/\gamma\Omega = 0.039$ s. For the stabilizer bar, with its small aerodynamic surfaces, the Lock number is low, $\gamma_{tb} \approx 0.8$, and the corresponding settling time is 0.144 s. Earlier work on modeling of small-scale rotorcraft with Bell-Hiller stabilizer bars (Mettler et al. 2002b; Mettler 2002; LaCivita et al. 2002b) showed that the main rotor and stabilizer bar flapping dynamics can be lumped and represented by tip-path plane (TPP) flapping dynamics with only two states. This result was based on frequency-domain identification and comparison of reduced and full order transfer functions for attitude dynamics. Furthermore, coupling of the lumped flapping dynamics and rigid body pitch and roll motions leads to pronounced second-order characteristics (von Grunhagen et al. 1996; Talbot et al. 1982; Mettler 2002; LaCivita et al. 2002b). These modes are lightly damped and should be explicitly accounted for in designing high-bandwidth attitude or rate control systems (Mettler et al. 2000, 2002a). The lateral and longitudinal flapping dynamics were represented by the first-order equations:

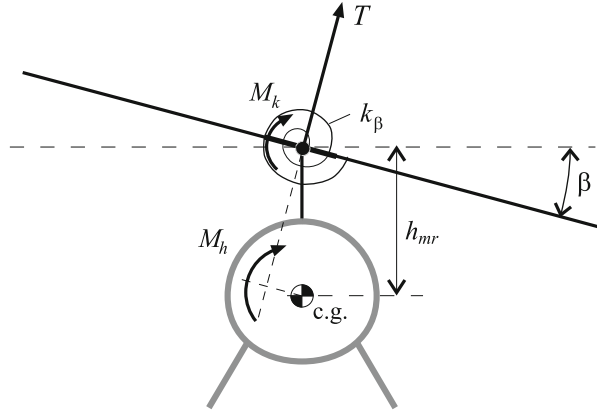
$$\dot{b}_1 = -p - \frac{b_1}{\tau_e} - \frac{1}{\tau_e} \frac{\partial b_1}{\partial \mu_v} \frac{v - v_w}{\Omega R} + \frac{B_{\delta_{lat}}}{\tau_e} \delta_{lat} \quad (15.17)$$

$$\dot{a}_1 = -q - \frac{a_1}{\tau_e} + \frac{1}{\tau_e} \left(\frac{\partial a_1}{\partial \mu} \frac{u - u_w}{\Omega R} + \frac{\partial a_1}{\partial \mu_z} \frac{w - w_w}{\Omega R} \right) + \frac{A_{\delta_{lon}}}{\tau_e} \delta_{lon} \quad (15.18)$$

where $B_{\delta_{lat}}$ and $A_{\delta_{lon}}$ are effective steady-state lateral and longitudinal gains from the cyclic inputs to the main rotor flap angles; δ_{lat} and δ_{lon} are the lateral and longitudinal cyclic control inputs (pilot stick or control system outputs); u_w , v_w , and w_w are the wind components along, respectively, X, Y, and Z helicopter body axes; and τ_e is the effective rotor time constant for a rotor with the stabilizer bar. Frequency-domain identification showed that the pitch and roll cross-coupling flapping coefficients are approximately an order of magnitude less than the direct coefficients for the X-Cell (Mettler 2002) and were neglected. This result holds for large-amplitude inputs as well. For example, during an axial roll maneuver, the pitch rate remains close to zero with no pilot compensation, similarly to the roll rate during a loop. This natural decoupling of the cyclic responses makes the X-Cell a particularly attractive helicopter for aerobatics.

The dominant rotor moments are the control moments produced by the rotor flapping. In the following pages, the moments in the roll direction are described (resulting from the lateral TPP flapping b_1). Figure 15.4 shows the rotor moments that are acting on the fuselage. The first contribution results from the restraint in the blade attachment to the rotor head. The restraint can be approximated using a linear torsional spring with a constant stiffness coefficient K_β , resulting in a roll moment $M_{k,lat} = K_\beta b_1$. The second contribution results from the tilting of the thrust vector. Assuming that the thrust vector is perpendicular to the TPP, the thrust vector will tilt proportionally to the rotor flapping angles. The moment arm is the distance h_{mr}

Fig. 15.4 Rotor moments acting on the helicopter fuselage



between the rotor head and the helicopter center of gravity, resulting in a lateral moment $M_{h,lat} = T h_{mr} b_1$. The total main rotor rolling moment, entering the rigid body equations of motion, is represented by Eq. (15.19):

$$L_{mr} = (K_\beta + T h_{mr}) b_1 \quad (15.19)$$

Similarly, the pitching moment is given by Eq. (15.20):

$$M_{mr} = (K_\beta + T h_{mr}) a_1 \quad (15.20)$$

To determine the parameters entering the flapping equations, one can split up the problem into “slow” and “fast” dynamics. First, one can notice that the dihedral derivatives are important only at the low-frequency spectrum of the dynamics. At high frequencies (above 0.5 Hz), the transfer functions from cyclic inputs to angular rates can be approximated by second-order transfer functions, derived by omitting the translational flapping derivatives in Eqs. (15.17) and (15.18) and combining it with Eqs. (15.19) and (15.20):

$$\frac{q}{\delta_{lon}} \approx \frac{A_{\delta_{lon}}}{\tau_e} \frac{\omega_{nq}^2}{s^2 + 1/\tau_e s + \omega_{nq}^2} \quad (15.21)$$

$$\frac{p}{\delta_{lat}} \approx \frac{B_{\delta_{lat}}}{\tau_e} \frac{\omega_{np}^2}{s^2 + 1/\tau_e s + \omega_{np}^2} \quad (15.22)$$

Pitching dynamics in fast forward flight is significantly influenced by the horizontal tail, which provides a stabilizing effect, and the main rotor flapping due to vertical speed, which provides a destabilizing effect. Therefore, the longitudinal cyclic to pitch rate transfer function given in Eq. (15.21) is valid in low-speed flight only. Here the undamped natural frequencies of the longitudinal and lateral fuselage-rotor modes are

$$\omega_{nq} = \sqrt{\frac{T_{mr}h_{mr} + K_\beta}{I_{yy}}}$$

$$\omega_{np} = \sqrt{\frac{T_{mr}h_{mr} + K_\beta}{I_{xx}}}$$

Note that for hover and straight and level flight, $T_{mr} \approx mg$. The distance between the main rotor hub and the helicopter center of gravity can be measured. The moments of inertia were determined with the torsional pendulum tests (Harris 1996). The natural frequencies of the lightly damped second-order systems can be easily determined by counting oscillation periods in a recorded step response, thereby providing an estimate of the hub torsional stiffness. These parameters are given in Table 15.1. An approximate value of the damping time constant for the flapping motion (Mettler 2002) is given in Eq. (15.23):

$$\tau_e = \frac{16}{\gamma_{fb}\Omega_{mr}} \approx 0.1 \text{ s} \quad (15.23)$$

Note that the damping is proportional to the stabilizer bar Lock number, making it small. The steady-state cyclic to rate gains depend on the swashplate gearing. Experiments have also indicated that the values of $B_{\delta_{lat}}$ and $A_{\delta_{lon}}$ grow with the rotor speed. This effect was approximated as a function of effective dynamic pressure, or square of the rotor speed:

$$B_{\delta_{lat}} = B_{\delta_{lat}}^{\text{nom}} \left(\frac{\Omega}{\Omega_{\text{nom}}} \right)^2 \text{ rad/rad}$$

$$A_{\delta_{lon}} = A_{\delta_{lon}}^{\text{nom}} \left(\frac{\Omega}{\Omega_{\text{nom}}} \right)^2 \text{ rad/rad}$$

$$\Omega_{\text{nom}} = 167 \text{ rad/s}$$

These gains were determined by matching DC gain of the angular rate responses to steps in cyclics. Final verification of the derived parameters is provided by simulation of the linear systems described in Eqs. (15.21) and (15.22) and comparison with the flight-test data. Figure 15.5 shows the actual and simulated roll rates for a segment including an axial roll maneuver. The helicopter undergoes negative rotor loading during inverted portion of the maneuver, leading to 15% lower roll rate in that segment than predicted by the simplified linear model. Figure 15.6 shows the actual and simulated pitch rates for a segment of 15 m/s forward flight with pulse commands on longitudinal cyclic. Note that the linearized models of angular rate dynamics are adequate for both small- and large-amplitude motion.

The flapping due to translational velocity is described by the flapping derivatives $\partial a_1/\partial \mu$ and $\partial b_1/\partial \mu_v$. The longitudinal flapping due to the forward speed increase

Fig. 15.5 Actual and model roll rate response during axial roll maneuver

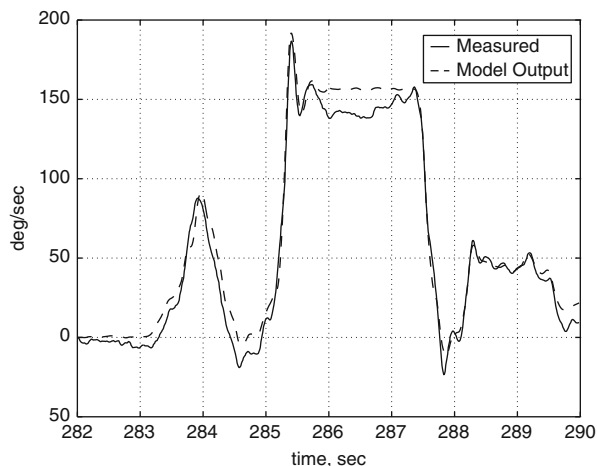
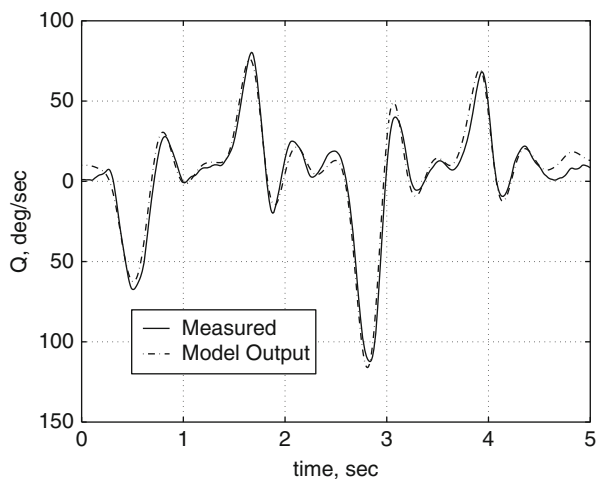


Fig. 15.6 Actual and model pitch rate response in low-speed flight



is caused by an increased lift on the advancing blade with respect to the retreating blade, which turns into a flap-back moment on the main rotor due to the 90° gyroscopic phase lag. A theoretical value for the steady-state longitudinal flapping for a rotor without a stabilizer bar is given by Bramwell (2001, p. 107)

$$a_1 = \frac{2\mu (4\delta_{\text{col}}/3 - \lambda_0)}{1 + 3\mu^2/2} \approx 2\mu (4\delta_{\text{col}}/3 - \lambda_0) \quad (15.24)$$

While this expression is valid for a teetering rotor at hover, theoretical approximation for a hingeless rotor without a stabilizer bar is very close (Padfield 1996). The stabilizer bar dramatically reduces flapping response to gusts, and

Eq. (15.24) cannot be used for predicting dihedral effect on a rotor equipped with one. Since this derivative plays a primary role in the frequency and damping of the phugoid mode, which is very slow, it is difficult to estimate with the frequency-domain identification methods (Mettler 2002). An open loop excitation would have to last for much longer than it takes for the helicopter to diverge; therefore, the necessary pilot's feedback would bias an estimate of the derivative (Ljung 1999). A scaling coefficient was introduced in Eq. (15.24), which was linearized to yield

$$\frac{\partial a_1}{\partial \mu} = 2K_\mu \left(\frac{4\delta_{\text{col}}}{3} - \lambda_0 \right) \quad (15.25)$$

A rough estimate for the scaling coefficient K_μ can be obtained by matching the steady-state cyclic input in forward flight at constant speed (maintained with the velocity-tracking feedback controller) with that predicted by the simulation in the same conditions. An estimate for X-Cell 60 yielded $K_\mu = 0.2$, which implies that the stabilizer bar reduces steady-state flapping response to forward speed by a factor of 5. From Eq. (15.24) and the rotor symmetry, one can conclude that the longitudinal and lateral dihedral derivatives are equal in magnitude and, in both cases, cause the rotor to flap away from the incoming air:

$$\frac{\partial b_1}{\partial \mu_v} = -\frac{\partial a_1}{\partial \mu} \quad (15.26)$$

Positive Z-axis velocity causes higher lift on advancing blade, which results in a flap back of the rotor; this effect is captured by the stability derivative $\partial a_1 / \partial \mu_z$ in Eq. (15.17). An analytical estimate of the derivative is adapted (Bramwell 2001, p. 159) to accommodate backward flight and scaled by the same coefficient K_μ to reflect the effect of the stabilizer bar:

$$\frac{\partial a_1}{\partial \mu_z} = K_\mu \frac{16\mu^2}{(1 - \mu^2/2)(8|\mu| + a\sigma)} \text{sign } \mu \approx K_\mu \frac{16\mu^2}{8|\mu| + a\sigma} \text{sign } \mu \quad (15.27)$$

15.4.1.4 Rotor Forces

For small advance ratio flight ($\mu < 0.15$), one can assume that the thrust vector is perpendicular to the TPP. The small flapping angles (below 10°) allow one to use linear approximation for the main rotor force components along the helicopter body axes. As was stated above, the in-plane rotor force was lumped with the fuselage forces and is not accounted for in the equations below:

$$X_{\text{mr}} = -T_{\text{mr}}a_1$$

$$Y_{\text{mr}} = T_{\text{mr}}b_1$$

$$Z_{\text{mr}} = -T_{\text{mr}}$$

15.4.2 Engine, Governor, and Rotor Speed Model

The rotor speed dynamics is modeled by the following equation:

$$\dot{\Omega} = \dot{r} + \frac{1}{I_{\text{rot}}} [Q_e - Q_{\text{mr}} - n_{\text{tr}} Q_{\text{tr}}] \quad (15.28)$$

where Q_e is the engine torque (positive clockwise), $Q_{\text{mr}} = C_Q \rho (\Omega R)^2 \pi R^3$ is the main rotor torque (positive counterclockwise), Q_{tr} is the tail rotor torque, n_{tr} is the tail rotor gear ratio, I_{rot} is the total rotating inertia referenced to the main rotor speed, and Ω is the rotor speed. The engine torque depends on the throttle setting δ_t and rotor speed and is usually represented by engine maps or lookup tables. The maps for the engine were not available, and a simplified representation of the engine torque is suggested. Assume that engine power is proportional to the throttle setting:

$$P_e = P_e^{\text{max}} \delta_t \quad (15.29)$$

where $0 < \delta_t < 1$. Then, the torque is

$$Q_e = \frac{P_e}{\Omega} \quad (15.30)$$

The engine torque response to throttle changes can be considered instantaneous, since the time lags associated with air intake, fuel flow, and combustion are very small compared to vehicle dynamics.

In the absence of manufacturer data, the governor can be modeled as a proportional-integral feedback controller, maintaining commanded rotor speed by changing the throttle:

$$\begin{aligned} \delta_t &= K_p \cdot (\Omega_c - \Omega) + K_i \cdot \omega_i \\ \dot{\omega}_i &= \Omega_c - \Omega \end{aligned} \quad (15.31)$$

where Ω_c is the rotor speed command and K_p and K_i are proportional and integral feedback gains. The anti-windup logic resets the integrator state value ω_i in case computed throttle command is saturated. Throttle servo dynamics is much faster than the rotor speed dynamics and was neglected in the model.

To determine the parameters of the given engine/governor model, time response to the rotor speed step command was analyzed. Consider linearization of Eqs. (15.28)–(15.31) around a nominal operating point, for example, hovering flight, neglecting the yawing acceleration and the tail rotor torque. The states of the linear system will be the rotor speed deviation from the nominal ω and an integral of the rotor speed tracking error ω_i . The inputs are ω_c , a variation of the rotor speed command, and δ_c , a variation of the collective angle from the trim setting. The resulting linear system is given in Eq. (15.32):

$$\begin{aligned} \frac{d}{dt} \begin{bmatrix} \omega \\ \omega_i \end{bmatrix} = & \begin{bmatrix} -\frac{1}{\Omega I_{\text{rot}}} (3Q_{\text{mr}}^0 + P_e^{\text{max}} K_p) & \frac{P_e^{\text{max}} K_i}{\Omega I_{\text{rot}}} \\ -1 & 0 \end{bmatrix} \begin{bmatrix} \omega \\ \omega_i \end{bmatrix} \\ & + \begin{bmatrix} \frac{P_e^{\text{max}} K_p}{\Omega I_{\text{rot}}} & -\frac{1}{I_{\text{rot}} C_Q} \frac{\partial C_Q}{\partial \delta_c} Q_{\text{mr}}^0 \\ 1 & 0 \end{bmatrix} \begin{bmatrix} \omega_c \\ \delta_c \end{bmatrix} \end{aligned} \quad (15.32)$$

From Eq. (15.11), the main rotor torque at hover Q_{mr}^0 can be computed, and for the X-Cell with the parameters given in Table 15.1, $Q_{\text{mr}}^0 \approx 6.3 \text{ Nm}$. The characteristic polynomial of the system is given in Eq. (15.33):

$$\chi(\lambda) = \lambda^2 + \lambda \frac{3Q_{\text{mr}}^0 + P_e^{\text{max}} K_p}{\Omega I_{\text{rot}}} + \frac{P_e^{\text{max}} K_i}{\Omega I_{\text{rot}}} \quad (15.33)$$

To estimate the coefficients of the characteristic polynomial, the following test was performed (Sprague et al. 2001). The helicopter was kept at hover at 1,600 rpm, and a 100 rpm step input in rotor speed was commanded to the governor from a remote control. The rotor speed measurement was not available directly in the instrumentation package. Instead, the sound of the engine was recorded with a handheld camcorder. Next, a time-frequency decomposition analysis (Feron et al. 1998) was applied to determine frequency content of the engine noise as a function of time. In such an analysis, a signal of limited duration and frequency, called a wavelet, defined by its central frequency and width, is convoluted in the time domain with the data. The output in the time domain will have a larger magnitude when the wavelet's central frequency is present in the signal than when the central frequency is missing. The spectral content of the signal as a function of time can then be determined by repeating this computation over a range of frequencies. Many frequency bands appear in the sound spectrum of the engine noise, representing harmonics. Figure 15.7 (top) shows the result of the Morlet wavelet time-frequency analysis performed on the engine noise during a step change in RPM setting; two harmonics are indicated. The same behavior appears on each harmonic, providing the opportunity to fine-tune the model to a number of step responses, thereby reducing measurement error due to external noise. The governor/engine system was approximated with a second-order system, whose response to a commanded RPM step input appears at the bottom of Fig. 15.7. The system's damping ratio is $\zeta = 0.63$, and its natural frequency is $\omega_n = 1.3 \text{ rad/s}$. By matching the coefficients of the characteristic polynomials, one can obtain the expressions given in Eq. (15.34):

$$\begin{aligned} 2\zeta\omega_n &= \frac{3Q_{\text{mr}}^0 + P_e^{\text{max}} K_p}{\Omega I_{\text{rot}}} \\ \omega_n^2 &= \frac{P_e^{\text{max}} K_i}{\Omega I_{\text{rot}}} \end{aligned} \quad (15.34)$$

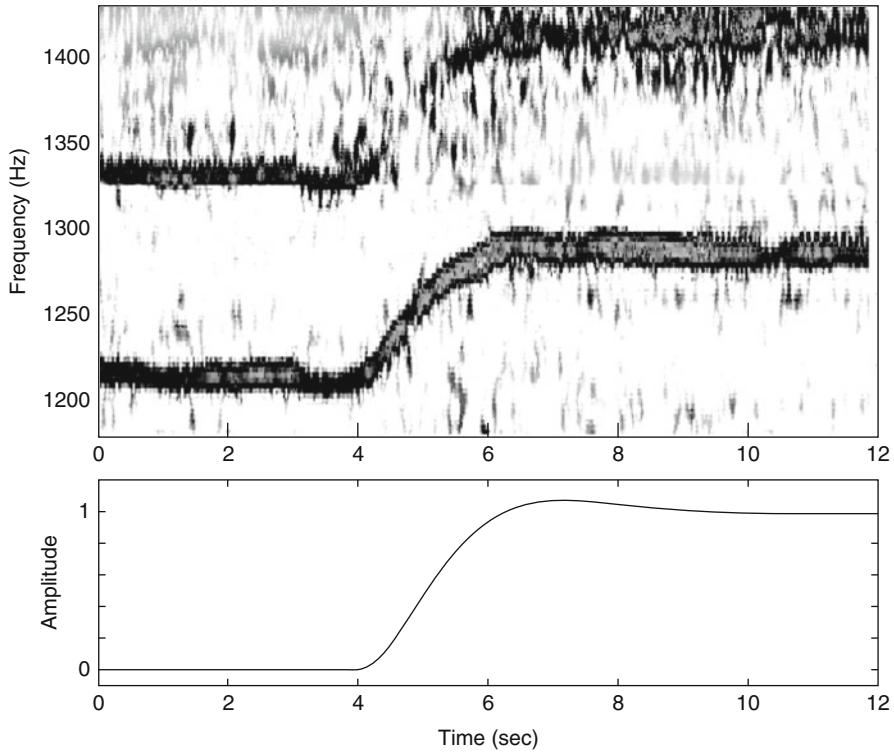


Fig. 15.7 (top) Two frequency bands in the engine noise spectrum; (bottom) simulated response to rotor speed step command

A total kinetic energy of all rotating components is $2I_{\beta_{mr}}\Omega^2 + I_{es}(n_{es}\Omega)^2 + 2I_{\beta_{tr}}(n_{tr}\Omega)^2 = (2I_{\beta_{mr}} + I_{es}n_{es}^2 + 2I_{\beta_{tr}}n_{tr}^2)\Omega^2$, where $I_{\beta_{mr}}$ and $I_{\beta_{tr}}$ are, respectively, the main and the tail rotor blade inertias, I_{es} is the inertia of the engine shaft and all components rotating at the engine speed, n_{tr} is the tail rotor gear ratio, and n_{es} is the engine gear ratio. Therefore, the rotating inertia referenced to the main rotor speed can be represented as $I_{rot} = 2I_{\beta_{mr}} + I_{es}n_{es}^2 + 2I_{\beta_{tr}}n_{tr}^2$. The most important contribution comes from the main rotor blades. The tail rotor inertia, after scaling with the gear ratio squared, amounts to 5 % of the main rotor inertia. The rotating inertia referenced to the engine speed is harder to estimate, but an upper bound can be found by estimating the total mass of rotating components (0.2 kg) and its effective radius of inertia (0.04 m). One thus arrives at an estimate for I_{rot} equal to 2.5 inertias of the main rotor blade. Using this value, and matching coefficients of the characteristic polynomial according to Eq. (15.34), estimates for the proportional and integral governor gains were obtained. The model could be further refined if real-time rotor speed data were available, or the actual governor gain and the engine maps were available from the manufacturer datasheets.

This engine/governor model is simplified. However, it reflects the trends which are important in some very aggressive maneuvers which involve large and rapid variation of the aerodynamic torque on the rotor. First, tight governor feedback keeps the rotor speed close to the nominal setting. Second, an increase in the aerodynamic torque leads to a temporary decrease in rotor speed and a lagged application of the yawing torque to the airframe. The reverse is true for windmilling flight, in which the rotor extracts energy from the air, and leads to an increase in rotor speed, and lagged decrease in torque applied to the airframe. The inaccuracies in the model can make feedforward compensation of the main rotor torque with the tail rotor difficult to tune; a tight yaw rate feedback to the tail rotor pitch is much more effective and is routinely used by R/C pilots in the form of a yaw rate gyro.

15.4.3 Fuselage Forces

For hover flight and forward speeds well below the induced velocity at hover (≈ 4.5 m/s for X-Cell), the rotor downwash is deflected by the forward and side velocity. This deflection creates a force opposing the movement. One can express the X and Y drag forces created by the fuselage in this flight regime by

$$X_{\text{fus}} = S_x^{\text{fus}} \frac{1}{2} \rho V_{\text{imr}}^2 \frac{u}{V_{\text{imr}}}$$

$$Y_{\text{fus}} = S_y^{\text{fus}} \frac{1}{2} \rho V_{\text{imr}}^2 \frac{v}{V_{\text{imr}}}$$

where S_x^{fus} and S_y^{fus} are effective drag areas of the fuselage in the X and Y directions.

When the forward speed is higher than the rotor induced velocity, the fuselage drag can be modeled as the drag of a flat plate exposed to dynamic pressure. In this case, the perturbations to the fuselage forces can be expressed as

$$X_{\text{fus}} = S_x^{\text{fus}} \frac{1}{2} \rho U_e^2 \frac{u}{U_e}$$

$$Y_{\text{fus}} = S_y^{\text{fus}} \frac{1}{2} \rho U_e^2 \frac{v}{U_e}$$

where U_e is the trim airspeed.

Considering the above equations, fuselage forces can be approximated by

$$V_{\infty} = \sqrt{u_a^2 + v_a^2 + (w_a + V_{\text{imr}})^2}$$

$$X_{\text{fus}} = -0.5 \rho S_x^{\text{fus}} u_a V_{\infty}$$

$$Y_{\text{fus}} = -0.5\rho S_y^{\text{fus}} v_a V_\infty$$

$$Z_{\text{fus}} = -0.5\rho S_z^{\text{fus}} (w_a + V_{\text{imr}}) V_\infty$$

where S_x^{fus} , S_y^{fus} , and S_z^{fus} are effective frontal, side, and vertical drag areas of the fuselage and u_a , v_a , and w_a are fuselage center of pressure velocities with respect to air (i.e., $u_a = u - u_w$, where u_w is the projection of wind velocity vector on the X body axis). One can neglect small moments generated by the fuselage and assume that the fuselage center of pressure coincides with the helicopter center of gravity. Based on the fuselage projection areas, one can assume that $S_y^{\text{fus}} \approx 2.2S_x^{\text{fus}}$, $S_z^{\text{fus}} \approx 1.5S_x^{\text{fus}}$. Effective frontal drag area can be determined from the average pitch angle required to maintain a certain forward speed. This is best done under automatic control in velocity hold mode. In a steady trimmed flight, $\text{mg}\theta \approx -0.5\rho U^2 S_x^{\text{fus}}$. A pitch angle of -10° was required to maintain 14.5 m/s forward speed, which resulted in the estimate $S_x^{\text{fus}} = 0.1 \text{ m}^2$.

15.4.4 Vertical Fin Forces and Moments

The side force generated by the vertical fin can be approximated as follows:

$$Y_{\text{vf}} = -0.5\rho S_{\text{vf}} (C_{L_\alpha}^{\text{vf}} V_\infty^{\text{tr}} + |v_{\text{vf}}|) v_{\text{vf}} \quad (15.35)$$

where S_{vf} is the vertical fin area, $C_{L_\alpha}^{\text{vf}}$ is its lift curve slope, $V_\infty^{\text{tr}} = \sqrt{u_a \cdot u_a + w_{\text{tr}} \cdot w_{\text{tr}}}$ is the axial velocity at the location of the tail rotor hub, v_{vf} is the side velocity relative to air at the location of the vertical fin, and w_{tr} is the vertical velocity (same as for the tail rotor):

$$v_{\text{vf}} = v_a - \epsilon_{\text{vf}}^{\text{tr}} V_{\text{itr}} - l_{\text{tr}} r \quad (15.36)$$

$$w_{\text{tr}} = w_a + l_{\text{tr}} q - K_\lambda \cdot V_{\text{imr}} \quad (15.37)$$

Here V_{itr} is the induced velocity of the tail rotor (see Eq. (15.50)), r is yaw rate, $\epsilon_{\text{vf}}^{\text{tr}}$ is the fraction of the vertical fin area exposed to full induced velocity from the tail rotor, l_{tr} is the vertical distance between the c.g. and tail rotor hub, which is about the same distance to the center of pressure of the vertical fin, V_{imr} is the main rotor induced velocity, and K_λ is the wake intensity factor, calculated in the tail rotor section.

To accommodate for stall of the vertical fin (McConley 1998), the absolute value of the vertical fin side force is limited by

$$|Y_{\text{vf}}| \leq 0.5\rho S_{\text{vf}} \left((V_\infty^{\text{tr}})^2 + v_{\text{vf}}^2 \right) \quad (15.38)$$

The vertical fin side force creates a yawing moment and a small rolling moment due to the offsets from the c.g.:

$$N_{vf} = -Y_{vf}l_{tr}$$

$$L_{vf} = Y_{vf}h_{tr}$$

15.4.5 Horizontal Stabilizer Forces and Moments

The destabilizing effect of the main rotor flapping due to vertical speed is offset by the weathervaning provided by the horizontal tailplane. The horizontal tail produces lift and a stabilizing pitching moment around the center of gravity. An effective vertical speed at the horizontal tail location is determined, assuming that the stabilizer may be fully or partially submerged in the downwash of the main rotor:

$$w_{ht} = w_a + l_{ht}q - K_\lambda \cdot V_{imr} \quad (15.39)$$

The same wake intensity factor is used for the horizontal fin as for the vertical fin and the tail rotor. Next, the Z-force generated by the horizontal stabilizer is determined according to

$$Z_{ht} = 0.5\rho S_{ht} (C_{L_\alpha}^{ht} |u_a| w_{ht} + |w_{ht}| w_{ht}) \quad (15.40)$$

where S_{ht} is the horizontal stabilizer area and $C_{L_\alpha}^{ht} = 3.0$ is its lift curve slope. To accommodate for the stall of the horizontal stabilizer (McConley 1998), the absolute value of the horizontal stabilizer lift is limited by

$$|Z_{ht}| \leq 0.5\rho S_{ht} (u_a^2 + w_{ht}^2) \quad (15.41)$$

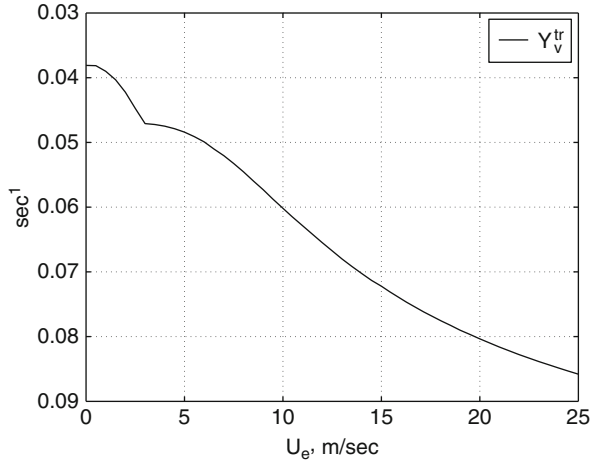
Finally, the pitching moment generated by the horizontal stabilizer is

$$M_{ht} = Z_{ht} \cdot l_{ht} \quad (15.42)$$

15.4.6 Tail Rotor

The tail rotor is subjected to a wide range of flow conditions, including those where the thrust-inflow iteration algorithm (given for the main rotor in Eqs. (15.4) and (15.5)) would fail (e.g., when the tail rotor operates in its own wake at a low in-plane airspeed). The thrust-inflow iteration equations for the tail rotor were linearized around the trim conditions corresponding to a no-sideslip flight at a range of forward speeds. The tail rotor thrust at such trim conditions is always nonzero to compensate for the main rotor torque, and zero sideslip implies that there is no airflow component normal to the rotor disk; therefore, Eqs. (15.4) and (15.5) are applicable:

Fig. 15.8 Linearized tail rotor side force due to side velocity



$$C_{T_{\mu_z}^{\text{tr}}} = \frac{\partial C_T^{\text{tr}}}{\partial \mu_z^{\text{tr}}} (|\mu_{\text{tr}}|, \mu_z^{\text{tr}} = 0, \delta_r^{\text{trim}}) \quad (15.43)$$

$$C_{T_{\delta_r}^{\text{tr}}} = \frac{\partial C_T^{\text{tr}}}{\partial \delta_r} (|\mu_{\text{tr}}|, \mu_z^{\text{tr}} = 0, \delta_r^{\text{trim}}) \quad (15.44)$$

The partial derivatives in Eqs. (15.43) and (15.44) were computed numerically. Simple approximate analytical expressions for the tail rotor coefficients can be obtained by adapting those used for the main rotor coefficients (Padfield 1996, pp. 219, 229). They fall within 15 % of those computed via numerical or exact analytical linearization. The resulting nondimensional coefficients were used to calculate the corresponding dimensional stability derivatives:

$$Y_v^{\text{tr}} = -C_{T_{\mu_z}^{\text{tr}}} \frac{f_t \rho \Omega_{\text{tr}} R_{\text{tr}} \pi R_{\text{tr}}^2}{m} \quad (15.45)$$

$$Y_{\delta_r}^{\text{tr}} = -C_{T_{\delta_r}^{\text{tr}}} \frac{f_t \rho (\Omega_{\text{tr}} R_{\text{tr}})^2 \pi R_{\text{tr}}^2}{m} \quad (15.46)$$

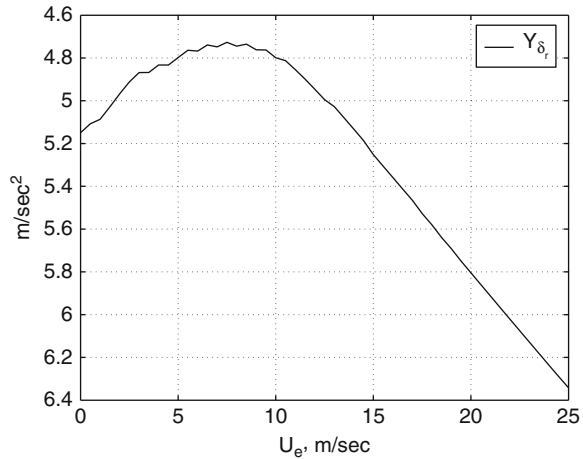
where f_t is the fin blockage factor, as suggested in Padfield (1996, p. 142):

$$f_t = 1.0 - \frac{3}{4} \frac{S_{\text{vf}}}{\pi R_{\text{tr}}^2}$$

The tail rotor speed is given by $\Omega_{\text{tr}} = n_{\text{tr}} \Omega_{\text{mr}}$, where n_{tr} is the gear ratio given in Table 15.1. For reference, the computed dimensional derivatives are provided in Figs. 15.8 and 15.9. Finally, the side force generated by the tail rotor is given in Eq. (15.47):

$$Y_{\text{tr}} = m Y_{\delta_r}^{\text{tr}} \delta_r + m Y_v^{\text{tr}} \mu_z^{\text{tr}} \Omega_{\text{tr}} R_{\text{tr}} \quad (15.47)$$

Fig. 15.9 Linearized tail rotor side force due to tail rotor pitch



In order to calculate Y_{tr} , one needs to determine the normal (μ_z^{tr}) and the in-plane (μ_{tr}) tail rotor inflow components. The main rotor wake affects the tail rotor thrust in a complex way; to model this influence accurately, an extensive modeling of the wake is required. It was decided to approximate just the increase in an apparent in-plane velocity seen by the tail rotor. For this, determine the main rotor wake intensity factor K_λ . The geometry calculations are equivalent to those given in Leishman (2000), but computationally more efficient since an explicit evaluation of the trigonometric functions is avoided. Calculate the following variables (tangents of the angles determining the geometry):

$$g_i = \frac{l_{tr} - R_{mr} - R_{tr}}{h_{tr}}$$

$$g_f = \frac{l_{tr} - R_{mr} + R_{tr}}{h_{tr}}$$

First, the tail rotor is out of the downwash if $V_{imr} \leq w_a$, in which case there is an effective upwash. Next, at low enough forward speed with respect to air, the tail rotor is out of the wake as well. This can be represented by the condition:

$$\frac{u_a}{V_{imr} - w_a} \leq g_i$$

In both of these cases, $K_\lambda = 0$. The tail rotor is fully in the wake if

$$\frac{u_a}{V_{imr} - w_a} \geq g_f \quad (15.48)$$

In the far wake, the downwash is twice the value at the rotor. It was assumed that $K_\lambda = 1.5$ when the tail rotor is fully immersed. In the remaining case, when the tail rotor is partially immersed, assume a linear growth of the wake intensity factor with the forward speed:

$$K_\lambda = 1.5 \frac{\frac{u_a}{V_{\text{mr}} - w_a} - g_i}{g_f - g_i} \quad (15.49)$$

The derived expression is used to calculate the vertical component of airspeed at the tail rotor location, as shown in Eq. (15.37). Next, determine an advance ratio for the tail rotor:

$$\mu_{\text{tr}} = \frac{u_a^2 + w_{\text{tr}}^2}{\Omega_{\text{tr}} \cdot R_{\text{tr}}}$$

Velocity component normal to the tail rotor is given by

$$v_{\text{tr}} = v_a - l_{\text{tr}} \cdot r + h_{\text{tr}} \cdot p$$

and in nondimensional form

$$\mu_{z_{\text{tr}}} = \frac{v_{\text{tr}}}{\Omega_{\text{tr}} \cdot R_{\text{tr}}}$$

The magnitude of the resulting tail rotor thrust is limited based on the assumed maximum thrust coefficient to model stall of the blades and other viscous losses:

$$Y_{\text{max}}^{\text{tr}} = f_t C_{T_{\text{max}}}^{\text{tr}} \rho (\Omega_{\text{tr}} R_{\text{tr}})^2 \pi R_{\text{tr}}^2$$

$$|Y_{\text{tr}}| \leq Y_{\text{max}}^{\text{tr}}$$

The yawing and small rolling moments due to offsets from the c.g. are computed as follows:

$$N_{\text{tr}} = -Y_{\text{tr}} l_{\text{tr}}$$

$$L_{\text{tr}} = Y_{\text{tr}} h_{\text{tr}}$$

The tail rotor induced velocity, used in the calculation of the vertical fin side force (see Eq. (15.36)), needs to be computed. Using the same derivation as for the main rotor (Padfield 1996, pp. 115–123), the inflow ratio is approximated by Eq. (15.50):

$$\lambda_0^{\text{tr}} = \mu_{z_{\text{tr}}} - 2 \left[\frac{2C_T^{\text{tr}}}{a_{\text{tr}} \sigma_{\text{tr}}} - \delta_r \left(\frac{1}{3} + \frac{\mu_{\text{tr}}^2}{2} \right) \right] \quad (15.50)$$

where C_T^{tr} is the computed tail rotor thrust coefficient, a_{tr} is the tail rotor blade lift curve slope given in Table 15.1, and $\sigma_{\text{tr}} = \frac{2C_{\text{tr}}}{\pi R_{\text{tr}}}$ is the tail rotor solidity ratio.

Finally, the tail rotor torque Q_{tr} is computed similarly to Eqs. (15.11) and (15.12) using the tail rotor parameters in place of the main rotor parameters.

15.5 Actuator Models

The command ranges for the cyclics and collective blade pitch are symmetric around the center point. The tail rotor blade pitch is offset by the trim value given in Table 15.1 such that the tail rotor pitch is computed as

$$\delta_r = \delta_r^{\text{cmd}} + \delta_r^{\text{trim}} \quad (15.51)$$

The following maximum commanded deflections were set, in radians:

$$\delta_{\text{lat}}^{\text{max}} = 0.096$$

$$\delta_{\text{lon}}^{\text{max}} = 0.096$$

$$\delta_{\text{col}}^{\text{max}} = 0.183$$

$$\delta_{r_{\text{cmd}}}^{\text{max}} = 0.38$$

Here $\delta_{\text{lat}}^{\text{max}}$ and $\delta_{\text{lon}}^{\text{max}}$ are actual maximum cyclic pitch angles of the main rotor blades, measured statically. The gearing between servos and pitch angles of control surfaces is close to being linear. Linear functions are used to relate servo pulse-width commands to control surface deflections. Lookup tables can be used for a different gearing. Hobby servos and pulse-width generation electronics used on the helicopter result in significant quantization effects. On average, 150 steps were used to encode rail-to-rail deflection of each control surface. This results, for example, in a tail rotor command quantization of 0.3° . Linear transfer functions are used to model the servo dynamics. Futaba S9402 servos, used for collective and cyclic deflections of the main rotor blades, were subjected to small-amplitude frequency sweeps under 35 oz-in mean load and small inertia, which was assumed to be representative of the actual loads experienced by the servos during the flight. The following transfer function came up as a result:

$$H_{\text{servo}}(s) = \frac{s/T_z + 1}{s/T_p + 1} \frac{\omega_n^2}{s^2 + 2\zeta\omega_n s + \omega_n^2}$$

where $T_z = 104$ s, $T_p = 33$ s, $\omega_n = 36$ rad/s, and $\zeta = 0.5$. Note that 90° phase lag occurs at roughly 30 rad/s, which also imposes a limitation on the control system bandwidth. A fast digital servo (Futaba S9450) was used for the tail rotor pitch. Since the torque required from the tail rotor servo is much lower than that required from the swashplate actuators, no-load small-signal bandwidth tests provide an

adequate model of the servo. As a result of the tests, the servo transfer function was approximated by a second-order system with the undamped natural frequency of 7 Hz and the damping ratio of 0.6.

Conclusion

A representative nonlinear dynamic model of a miniature aerobatic helicopter was developed with first-principles methods. In addition to the rigid body states, the model includes two states to represent lateral and longitudinal flapping angles of the main rotor, one state for the main rotor speed, and one state for the integral of the main rotor speed tracking error. Flight-test data were used for determining several key parameters. The model is valid up to advance ratios $\mu < 0.15$ for a variety of maneuvering flight conditions, including negative rotor loading and high angular rates. The model can be used for developing and evaluating control design methods for demanding tasks, including aerobatics. This simplified modeling framework is suitable for a class of miniature helicopters with hingeless rotors.

References

- P. Abbeel, A. Coates, A.Y. Ng, Autonomous auto-rotation of an rc helicopter, in *Proceedings of ISER*, Athens, Greece, 2008
- P. Abbeel, A. Coates, A.Y. Ng, Autonomous helicopter aerobatics through apprenticeship learning. *Int. J. Robot. Res.* **29**, 1608–1639 (2010)
- P. Abbeel, V. Ganapathi, A.Y. Ng, Learning vehicular dynamics with application to modeling helicopters, in *Proceedings of NIPS 18*, Vancouver, British Columbia, Canada, 2006
- A.R.S. Bramwell, *Bramwell's Helicopter Dynamics* (AIAA, Reston, 2001)
- R.T. Chen, A simplified rotor system mathematical model for piloted flight dynamics simulation. Technical Memorandum 78575, NASA, 1979
- E. Feron, M. Brenner, J. Paduano, A. Turevskiy, Time-frequency analysis for the transfer function estimation and application to flutter clearance. *AIAA J. Guid. Control Dyn.* **21**(3), 375–382 (1998)
- V. Gavrillets, Autonomous aerobatic maneuvering of miniature helicopters. Ph.D. dissertation, Massachusetts Institute of Technology, 2003
- V. Gavrillets, M. Martinos, B. Mettler, E. Feron, Control logic for automated aerobatic flight of miniature helicopter, in *Proceedings of the AIAA Guidance, Navigation, and Control Conference*, Monterey, CA, Aug 2002
- F.D. Harris, Articulated rotor blade flapping motion at low advance ratio. *J. Am. Helicopter Soc.* **17**, 41–48 (1972)
- C. Harris (ed.), *Shock and Vibration Handbook* (McGraw-Hill, New York, 1996)
- A.M. Kuethe, C.Y. Chow, *Foundations of Aerodynamics* (Wiley, New York, 1986)
- M. LaCivita, T. Kanade, G. Papageorgiu, W. Messner, Design and flight testing of a high-bandwidth h-infinity loop shaping controller for a robotic helicopter, in *Proceedings of the AIAA Guidance, Navigation, and Control Conference*, Monterey, CA, Aug 2002a
- M. LaCivita, W. Messner, T. Kanade, Modeling of small-scale helicopters with integrated first-principles and integrated system identification techniques, in *Presented at 58th Forum of American Helicopter Society*, Montreal, Canada, June 2002b
- J.G. Leishman, *Principles of Helicopter Aerodynamics* (Cambridge University Press, New York, 2000)
- L. Ljung, *System Identification: Theory for the User* (Prentice Hall, Upper Saddle River, 1999)

- M. McConley, Draper small autonomous aerial vehicle dynamic model. Technical report E41-98-091, Draper Laboratory, Aug 1998
- B. Mettler, *Identification, Modeling and Characteristics of Miniature Rotorcraft* (Kluwer, Boston, 2002)
- B. Mettler, M. Tischler, T. Kanade, W. Messner, Attitude control optimization for a small-scale unmanned helicopter, in *AIAA Guidance, Navigation and Control Conference*, Denver, CO, Aug 2000
- B. Mettler, V. Gavrillets, E. Feron, T. Kanade, Dynamic compensation for high-bandwidth control of small-scale helicopter, in *American Helicopter Society Specialist Meeting*, San Francisco, CA, Jan 2002a
- B. Mettler, M.B. Tischler, T. Kanade, System identification modeling of a small-scale unmanned rotorcraft for control design. *J. Am. Helicopter Soc.* **47**(1), 50–63 (2002b)
- Miniature Aircraft USA, *X-Cell .60 graphite SE Helicopter Kit (Special Edition) Instruction Manual* (Miniature Aircraft USA, Orlando, 1999)
- NASA Ames Research Center, *Comprehensive Identification from Frequency Responses: An Interactive Facility for System Identification and Verification* (NASA Ames Research Center, Moffet Field, 2000)
- G.D. Padfield, *Helicopter Flight Dynamics: The Theory and Application of Flying Qualities and Simulation Modeling*. AIAA Education Series (AIAA, Reston, 1996)
- J.M. Rolfe, K.J. Staples, *Flight Simulation*. (Cambridge University Press, Cambridge, 1986)
- K. Sprague, V. Gavrillets, D. Dugail, B. Mettler, E. Feron, Design and applications of an avionics system for a miniature acrobatic helicopter, in *AIAA Digital Avionics Systems Conference*, Daytona Beach, FL, 2001
- T.D. Talbot, B.E. Tingling, W.A. Decker, R.T. Chen, A mathematical model of a single main rotor helicopter for piloted simulation. Technical Memorandum 84281, NASA, 1982
- M. Tischler (ed.), *Advances in Aircraft Flight Control* (Taylor and Francis, Cornwall, 1996)
- W. von Grunhagen, G. Bouwer, H.-J. Pausder, F. Henchel, J. Kaletka, A high bandwidth control system for the helicopter in-flight simulator at the – modelling, performance and applications, in *Advances in Aircraft Flight Control*, ed. by M. Tischler (Taylor and Francis, Cornwall, 1996)